applied sciences

MDPI

Article

Design Optimization of the Magnet-Free Synchronous Homopolar Motor of a Subway Train

Vladimir Dmitrievskii [1], Vladimir Prakht [1,*], Vadim Kazakbaev [1] and Alecksey Anuchin [2]

[1] Department of Electrical Engineering, Ural Federal University, 620002 Yekaterinburg, Russia
[2] Department of Electric Drives, Moscow Power Engineering Institute, 111250 Moscow, Russia
* Correspondence: va.prakht@urfu.ru; Tel.: +7-909-028-49-25

Featured Application: The presented results can be used in designing of synchronous homopolar machines and traction electrical drives.

Abstract: Synchronous homopolar motors have no permanent magnets and their excitation winding is fixed at their stator. However, they can be a good alternative to induction and permanent magnet motors in traction applications requiring a wide constant power speed range. They provide an excitation flux control and a highly reliable brushless rotor design. This article presents the procedure and results of optimizing a 370 kW synchronous homopolar motor for driving subway train. The optimization procedure was developed to take into account the subway train moving trajectory. The analysis considers only a limited number of steady-state operating points of the motor to reduce computation time. The optimization results show a significant improvement of the target parameters of the traction drive. The optimization makes it possible to significantly reduce the losses in the operating cycle, as well as the torque ripple of the motor and the current rating of the traction inverter.

Keywords: synchronous homopolar motor; electrically excited synchronous motor; Nelder–Mead method; optimal design of electric machines; subway train; constant power speed range; traction drive

Citation: Dmitrievskii, V.; Prakht, V.; Kazakbaev, V.; Anuchin, A. Design Optimization of the Magnet-Free Synchronous Homopolar Motor of a Subway Train. *Appl. Sci.* **2022**, *12*, 12647. https://doi.org/10.3390/app122412647

Academic Editors: Loránd Szabó and Feng Chai

Received: 16 November 2022
Accepted: 8 December 2022
Published: 9 December 2022

1. Introduction

The interior permanent magnet synchronous motors (PMSM) are widespread in electric traction. The excitation of such motors is made by means of rear-earth magnets. Thus, these motors have high power-to-weight ratio and high efficiency [1,2]. However, PMSMs have the following disadvantages. (1) PMSMs have high cost due to presence of expensive rear-earth magnets. (2) The use of rear-earth magnets causes the dependence on the limited number of the magnet suppliers in the production chain [3]. The prices of the rear-earth magnets are unstable and can seriously vary over time in a few years [4,5]. (3) The extraction of rear-earth elements, which are used in production of the magnets, harms the environment [6]. (4) Permanent magnets are prone to irreversible demagnetization due to the high operating temperature of more than 120 °C and strong demagnetization field, inherent in a traction motor with limited dimensions. (5) PMSMs have high power loss at a rotational speed close to or equal to the maximum in the field weakening region due to a large stator winding current required to compensate the uncontrolled magnetomotive force (MMF) of permanent magnets [7–9]. (6) The presence of high electromotive force (EMF) in the windings during rotation can results in fire in case of short-circuiting. This is very dangerous particularly in subway and trains, those have huge kinetic energy and cannot stop immediately. In case of subway train, the probability of fire should be excluded at all due to the limited volume in the tunnel and difficultness of evacuation. Therefore, utilization of the PMSMs in such applications is undesirable.

The highlighted disadvantages of PMSMs with rear-earth magnets limit their applications in subway, trams, mining trucks, etc. To overcome these disadvantages of PMSMs the leading car manufactures such as BMW (models BMW iX3) and Renault (models Renault Zoe, Fluence, Megane E-TECH) have developed DC-excited synchronous motors (DCESM) with the excitation winding on the rotor (BMW [10,11], Renault [12]). The constant power speed range is provided by means of the flux regulation of DCESM [13,14]. However, the electrical machines of BMW iX3 and Renault Zoe have the slip rings and a brushed contact to feed the excitation winding on the rotor, which limits the motor speed and reduces its reliability [14].

An alternative could be high-reliable and brushless synchronous homopolar machines (SHM) having both excitation and power winding on stator, and a salient-pole rotor. The main advantages of SHMs compared to DCESMs are highly reliable brushless rotor design and concentrated excitation winding, the number of coils of which is small and does not depend on the number of motor poles, while in a DCESM the number of coils (and, therefore, the length of the wire and losses) increase with the number of poles. Such SHMs are widely used as the high-reliable generators in passenger railway cars, on-board generators for ships and aircraft [15,16], automotive generators [17], and in welding units [18].

In papers [7,19–23], the SHM is used as a traction motor of a mining truck. In [19], the simplified computation method of the traction SHM was described, and the experimental verification of the proposed method was performed. In [20], the control strategy of such traction motor was considered. In [21], this machine was optimized by means of the developed optimization procedure, which is now used at the design stage of the new motors. In [22], the optimization was made in order to minimize the installed power of the traction inverter of the mining truck. In [7], the parameters of the SHM are compared with the interior permanent magnet synchronous motor of the same power driving the same mining truck. In [23], the parameters of the SHM are compared with the parameters of the DCESM in the same application.

However, the review shows absence of use of SHM in other traction applications. This paper considers an optimization process for the synchronous homopolar motor for a traction electric drive of a subway train. The optimization was performed with respect to the typical speed and torque profile during transition between station considering acceleration and deceleration phases. The following optimization targets were selected: decrease in average losses along the way from station to station, decrease in installed power capacity of the traction inverter, and reduction of the torque ripple.

The one-criterion Nelder–Mead method is applied in this study to optimize the SHM design. An important advantage of the Nelder–Mead method over other methods that are often used to optimize electrical machines [24–28] is the significant savings in computational time, which makes it possible to increase the number of parameters to optimize, as well as to apply more complex optimization criteria, for the calculation of which it is necessary to calculate several load points of the machine [22]. This advantage is important for optimizing traction machines.

The optimization procedure was developed that takes into account the subway train moving trajectory. This analysis considers only a limited number of operating points making it possible to optimize the motor according to the specified cost function. The optimization results show a significant improvement in the target parameters of the traction drive.

2. Main Design Parameters of the SHM

Figure 1 shows the considered SHM design. The SHM has two stacks on the stator and two stacks on the rotor made of laminated steel. The stator stack and the rotor stack located in the front of the stator stack form the stator-rotor stack combination (SRSC). The stator lamination has 60 slots and 8-pole winding with a number of slots per pole and phase $q = 60/(8 \cdot 3) = 2.5$. The laminations are assembled from sheets of electrical steel 0.5 mm thick.

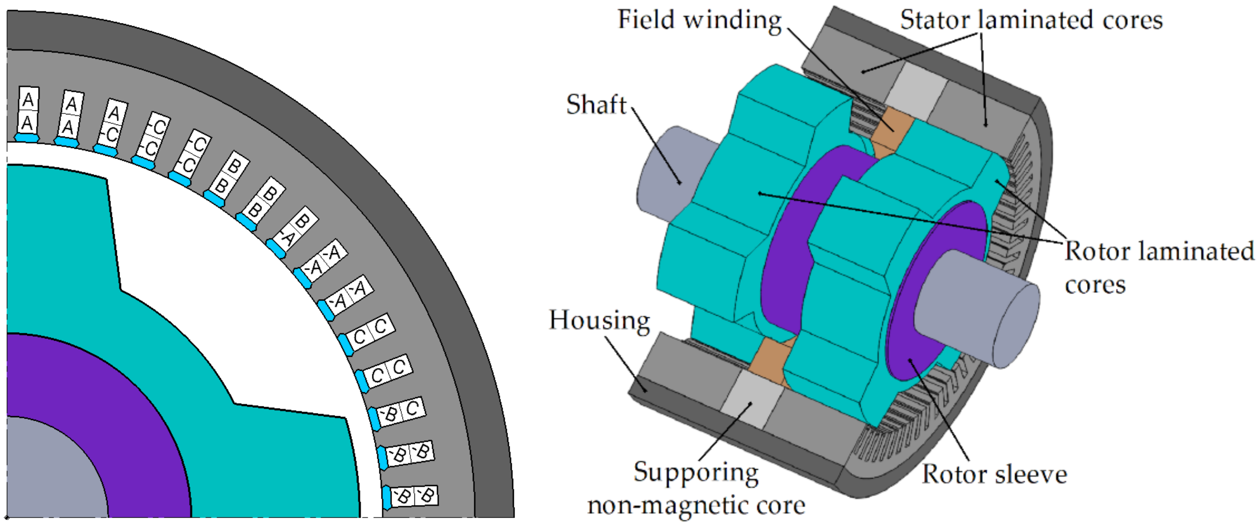

(**a**) (**b**)

Figure 1. Sketch of the SHM geometry: (**a**) Cross-section and stator power winding configuration (1/4 of the motor cross-section is shown, the other parts are symmetrical). (**b**) General view. The stator winding is not shown to avoid cluttering up the figure.

An excitation winding is located between the SRSCs. The rotor has no windings. Each rotor stack has 4 teeth, and the teeth of the rotor stacks are shifted by 45 mechanical degrees with respect to each other. The SHM housing and the rotor sleeve carry the stator lamination and the rotor lamination, respectively. They are made of a solid (not laminated) steel and provide the link to the flux produced by the excitation winding. No standard regulates the magnetic properties of solid steels, and, therefore, they can have significant dispersion. To guarantee that the housing and the sleeve are able to conduct the required flux, the flux density in these parts is restricted with the value of 1.6 T.

Figure 2 shows the inverter circuit diagram for powering the considered traction motor. To control the three-phase winding, field-oriented control is used, in which the stator current vector is formed in a coordinate system rotating synchronously with the rotor. The excitation winding current is set using PWM proportional to the armature current. The offset angle of the armature current vector from the direction of the greatest magnetic conductivity of the rotor pole for various operating points and the ratio between the armature current and the excitation current are reported in Section 6.

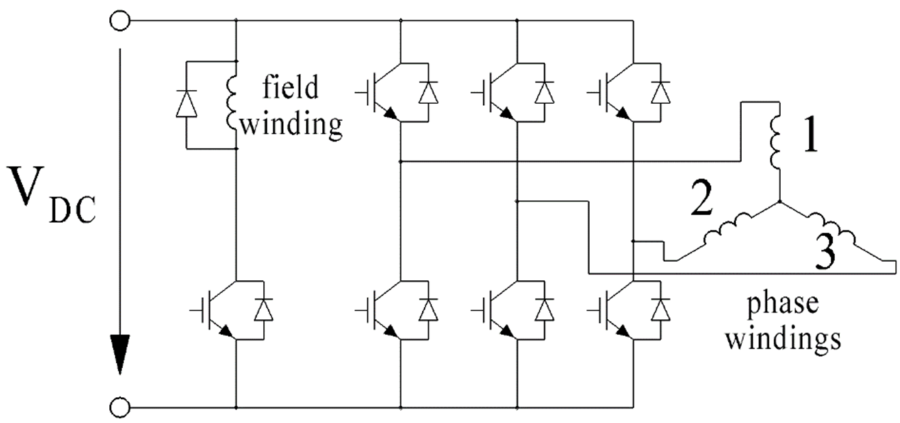

Figure 2. Schematics of the three-phase inverter with a DC-chopper for the excitation winding.

3. Operating Cycle and Operating Points of the Subway Train Motor

The transition of the train from one station to another has the following stages shown in Figure 3 [29]:

- Acceleration with the constant torque T_0;
- Acceleration with the constant power to maximum speed n_{max};
- Coasting with slow deceleration due to friction or movement with constant speed (cruising);
- Braking with the constant power;
- Braking with the constant torque T_0.

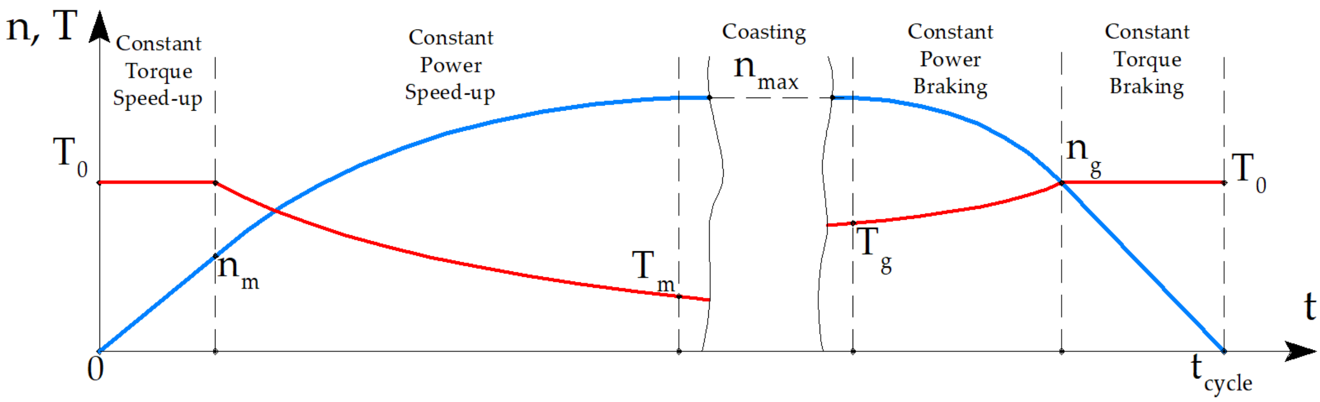

Figure 3. Sketch of the speed (blue) and torque (red) profiles in time of the traction motor of the subway train.

The considered powertrain is designed with the supercapacitors to store the energy of the braking. The rated voltage of the DC catenary is 750 V ($V_{DC\ rated}$). It was chosen as the minimal voltage for supercapacitors, whereas the maximum voltage of supercapacitors is chosen to be 1050 V. The supercapacitors are feeding traction inverter directly. During the start of the drive, the supercapacitors can be fully charged or partially discharged but the control system tries to discharge them to 750 V at the end of the acceleration phase in order to be ready for braking. These circumstances define the limit the maximum phase-to-phase voltage of the motor during acceleration stage of 750 V. A higher voltage limit can be applied for the braking modes of the motor to perform more efficient braking.

The demanded speed-torque curve of the traction motor is depicted in Figure 4. The right part of the plot corresponds to the driving mode of operation, whereas the left part of the plot represents generating mode. For the sake of simplicity, the negative torque in the generator mode is shown in absolute values above zero. The motor must produce maximum torque T_0 = 1240 N·m and the maximum speed n_{max} = 4280 rpm.

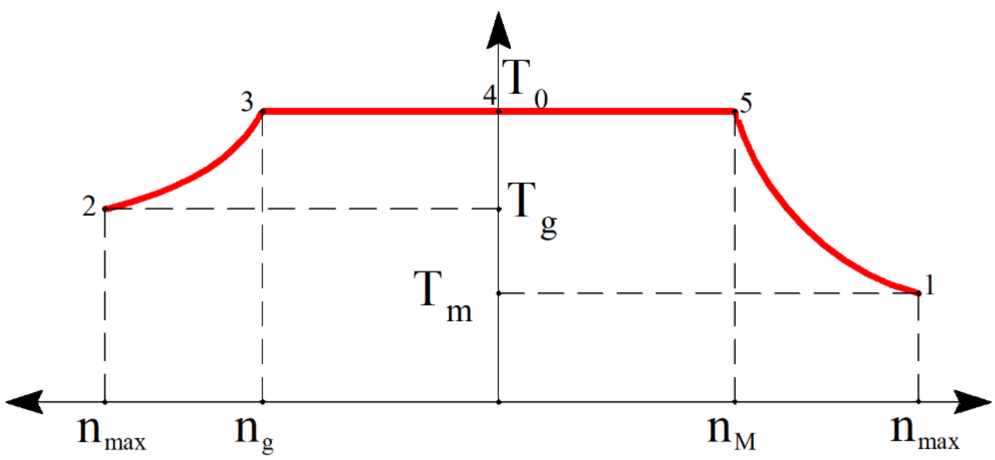

Figure 4. Demanded speed-torque curve of the subway traction drive.

The operation points in Figure 4 are enumerated in order of increasing torque:

1. Driving mode at the maximum speed n_{max};
2. Generating mode at the maximum speed n_{max};

3. Generating mode in the point of transition from constant power to constant torque at the speed n_g = 2854 rpm;
4. Zero speed mode with the maximum torque T_0 = 1240 N·m;
5. Driving mode at the point of transition from constant torque to constant power at the speed n_m = 1427 rpm.

4. Average Loss Calculation

Usually, the subway stations are located near of each other. Therefore, the duration of the cruising is not too much. Moreover, the required power in the cruising mode is much smaller than the one needed in other operation modes excluding stops. Therefore, the cruising mode and coasting were excluded from consideration.

Average value of some variable A during operation cycle depicted in Figure 4 is defined by equation:

$$< A >= \frac{\int\limits_{0}^{t_{cycle}} A dt}{t_{cycle}} = \frac{\int\limits_{cycle} A dt}{\int\limits_{cycle} dt} \tag{1}$$

where t_{cycle} is the duration of the cycle; t is time.

The mechanical subsystem of the train can be represented by:

$$J \frac{\mathrm{d}\Omega}{\mathrm{d}t} = \frac{2\pi}{60} J \frac{\mathrm{d}n}{\mathrm{d}t} = T \tag{2}$$

where Ω is the motor mechanical angular frequency in radians per second; $n = 60 \cdot \Omega / (2 \cdot \pi)$ is the motor rotational speed in revolutions per minute; J is the total equivalent inertia of the train at the motor shaft; T is the equivalent torque at the motor shaft. Neglecting the friction and the slopes, the equivalent torque T is equal to the torque produced by the motor.

By expressing dt from (2) and substituting it into (1) the average value can be expressed as:

$$< A > = \frac{\int\limits_{cycle} \frac{A}{T} dn}{\int\limits_{cycle} \frac{dn}{T}} \tag{3}$$

Let's estimate the value of integral in the numerator of (3) with a help of quadrature formulas. The operation mode of the motor changes in operation points 1–5 (see Figure 4), and there is no derivative of the torque with respect to speed. Therefore, it is reasonable to use the equation of first algebraic order (i.e., trapezoidal rule). Summing up the products of arithmetic means of the integrands A/T and the speed differences at the separate segments from Figure 4 (the segments from the point 2 to point 3, from 3 to 4, from 4 to 5, and from 5 to 1) results in the following:

$$\begin{aligned} \int\limits_{cycle} \frac{A}{T} dn \approx \left(\frac{A_2}{T_2} + \frac{A_3}{T_0} \right) \frac{n_{\max} - n_g}{2} + \left(\frac{A_3}{T_0} + \frac{A_4}{T_0} \right) \frac{n_g}{2} + \ldots \\ \ldots + \left(\frac{A_4}{T_0} + \frac{A_5}{T_0} \right) \frac{n_m}{2} + \left(\frac{A_5}{T_0} + \frac{A_1}{T_1} \right) \frac{n_{\max} - n_m}{2}, \end{aligned} \tag{4}$$

where A_1–A_5 are the values of the calculated function A at operating points 1–5 (see Table 1), respectively.

Table 1. Operating points of the traction motor considered during optimization.

Operating Point, i	Operating Point Name	Speed, rpm	Torque, N·m	w_i	k_i
1	Driving mode; maximum speed	4380	413.4	0.363	0.97
2	Generating mode; maximum speed	4380	826.9	0.091	0.99
3	Generating mode; transition from constant power to constant torque operation modes	2854	1240	0.182	1.1
4	Zero speed	0	1240	0.182	0.97
5	Driving mode; transition from constant torque to constant power operation modes	1427	1240	0.182	0.97

Approximation of the denominator of (3) can be expressed from (4) by substituting $A \equiv 1$. Substituting (4) into (3) as well as $T_2 = T_0 \cdot n_g/n_{max}$, $T_1 = T_0 \cdot n_m/n_{max}$, it is possible to find similarly summand in each product with A_i. Then the average loss estimation during operation cycle can be obtained as a weighted-average losses in points 1–5 of the operation cycle as:

$$< A > \approx \sum_{i=1,2,3,4,5} w_i A_i \tag{5}$$

In (5), the weight coefficients w_i normalized on the basis unity sum of all coefficients can be evaluated by:

$$w_i = \frac{W_i}{\sum\limits_1^5 W_i} \tag{6}$$

In (6), the coefficients Wi are calculated as according to (7):

$$W_1 = \frac{n_{\max}(n_{\max} - n_m)}{n_m};\ W_2 = \frac{n_{\max}(n_{\max} - n_g)}{n_g};\ W_3 = n_{\max};\ W_4 = (n_g + n_m);\ W_5 = n_{\max}. \tag{7}$$

Average value estimate (5) is relevant for any function $A(t)$ in the considered cycle from Figure 3. Here, this Equation (5) is used to evaluate average electric losses in the electric machine $<P_{loss\ el}>$. The losses during coasting are not taken into account due to the fact that they are small. Only the acceleration and deceleration phases are considered.

5. Voltage Limit

Kinetic energies of the train in operation points 2 and 3 (see Figure 4) equal to $J \cdot \Omega_{\max}{}^2/2$ and $J \cdot \Omega_g{}^2/2$, respectively. That is the train loses $1 - \Omega_g{}^2/\Omega_{\max}{}^2 = 1 - n_g{}^2/n_{max}{}^2$ part of its kinetic energy when braking from point 2 to 3. This energy is converted from the motion to the charge of the supercapacitor. The ratio between the energy accumulated in the supercapacitor during segment 2–3 and the total energy being accumulated at both segments 2–3 and 3–4 is $(V_3{}^2 - V_{DC\ rated}{}^2)/(V_{max}{}^2 - V_{DC\ rated}{}^2)$, where V_3 is the DC voltage in operating point 3; $V_{DC\ rated}$ is the rated voltage of the DC catenary; V_{max} is the maximum DC voltage. Therefore, the expected level of the DC link or supercapacitor voltage in the point 3 can be evaluated according to (8):

$$V_3 = \sqrt{V^2_{DC\ rated} + (V_3^2 - V^2_{DC\ rated})(1 - \frac{n_g^2}{n^2_{max}})} = 929\ \text{V}. \tag{8}$$

Thus, the desired motor phase-to-phase voltage amplitude V_i at operating points i = 1,2,3,4,5 can distinguish from $V_{DC\ rated}$ = 750 V. Table 1 shows the main parameters of the motor in the operation points i = 1,2,3,4,5, including weight coefficients being evaluated using (6) and normalized in addition to coefficient $k_i = V_i/V_{DC\ rated}$.

The expected DC voltage in the operation point 3 is 100%·(929 − 750)/750 = 24% higher than $V_{DC\ rated}$. Coefficient k_3 = 1.1 is selected with a large margin, and it is expected that the magnitude of the phase-to-phase voltage is higher than the rated voltage of the grid by 10% in the operating point 3. Moreover, a 3% margin for $V_{DC\ rated}$ is selected as the expected voltage drop across the power semiconducting switches in the driving mode, and a 1% margin for $V_{DC\ rated}$ is selected at operating point 2.

6. SHM Optimization Parameters and Procedure

Optimization of the motor parameters is performed using Nelder–Mead method. The Nelder–Mead algorithm used for the optimization is well known [30] and is included in the basic MATLAB software package (function "fminsearch"). This method is a one-criterion optimization method that uses only one objective function. The conventional approach for implementing multi-criteria optimization using a one-criterion method is to include in the optimized function all optimization objectives as a sum or product with certain weight coefficients [22].

The cost function is composed taking into account the following targets listed in descending order of importance:

1. Minimization of average losses $<P_{losses}>$;
2. Minimization of the maximum stator current magnitude during the entire operation cycle taking into account available voltage limit;
3. Minimization of the maximum symmetrized torque ripple along the entire operation cycle max ($TRsym$);
4. Minimization of the maximum non-symmetrized torque ripple along the entire operation cycle max(TR).

A non-symmetrized torque ripple is produced by a single SRSC. A symmetrized torque ripple is produced by a SHM as a whole. Details of TR and $TRsym$ are given in [19]. According to the targets of optimization the cost function can be written as their product. The weights are the powers to which the multipliers are raised:

$$\begin{gathered} F =< P_{loss\_el} > \max(I_i)^{0.7} \max(TRsym_i)^{0.025} \max(TR_i)^{0.01} f\left(\frac{\max(B_i)}{1.6[T]}\right), \\ f(x) = \begin{cases} 1, x < 1.6[T] \\ x^3, otherwise \end{cases}, \end{gathered} \tag{9}$$

where $<P_{loss\_el}>$ are the electric losses; I_i is the value of current in the ith operation point; $TRsym_i$ is the value of the symmetrized torque ripple in the ith operation point; TR is the value of the non-symmetrized torque ripple in the ith operation point, B_i the magnetic flux density in the housing and the sleeve.

The one-criterion Nelder–Mead method is applied in this study to optimize the SHM design. The Nelder–Mead method belongs to unconstrained optimization methods. The optimization constraints could be specified simply by assigning infinite values to the objective function when the constraint conditions are not met. However, this would lead to a rapid decrease in the volume of the simplex. For this reason, objective function (9) is modified by using the 'soft constraints' with the penalty growing rapidly in the forbidden area (if $B_i \geq 1.6$ T).

Optimization was performed neglecting the discrete nature of some parameters. The number of turns in the section of power winding N_{sec} is assumed to be a real number; it is not checked that the width and height was selected from the standard [31]. The number of turns is selected according to $V_{DC\ rated} = \max(V_i/k_i)$ [23]. The number of parallel branches is assumed to be equal to 4. Figure 5 shows the geometric parameters of the SHM.

The parameters fixed during the optimization and varied ones are given in Tables 2 and 3. Additionally, the areas of the cross-sections of the stator housing and the rotor sleeve are assumed to be equal since they transfer the same excitation flux. The shaft is assumed to be nonmagnetic or to have poor magnetic conductivity.

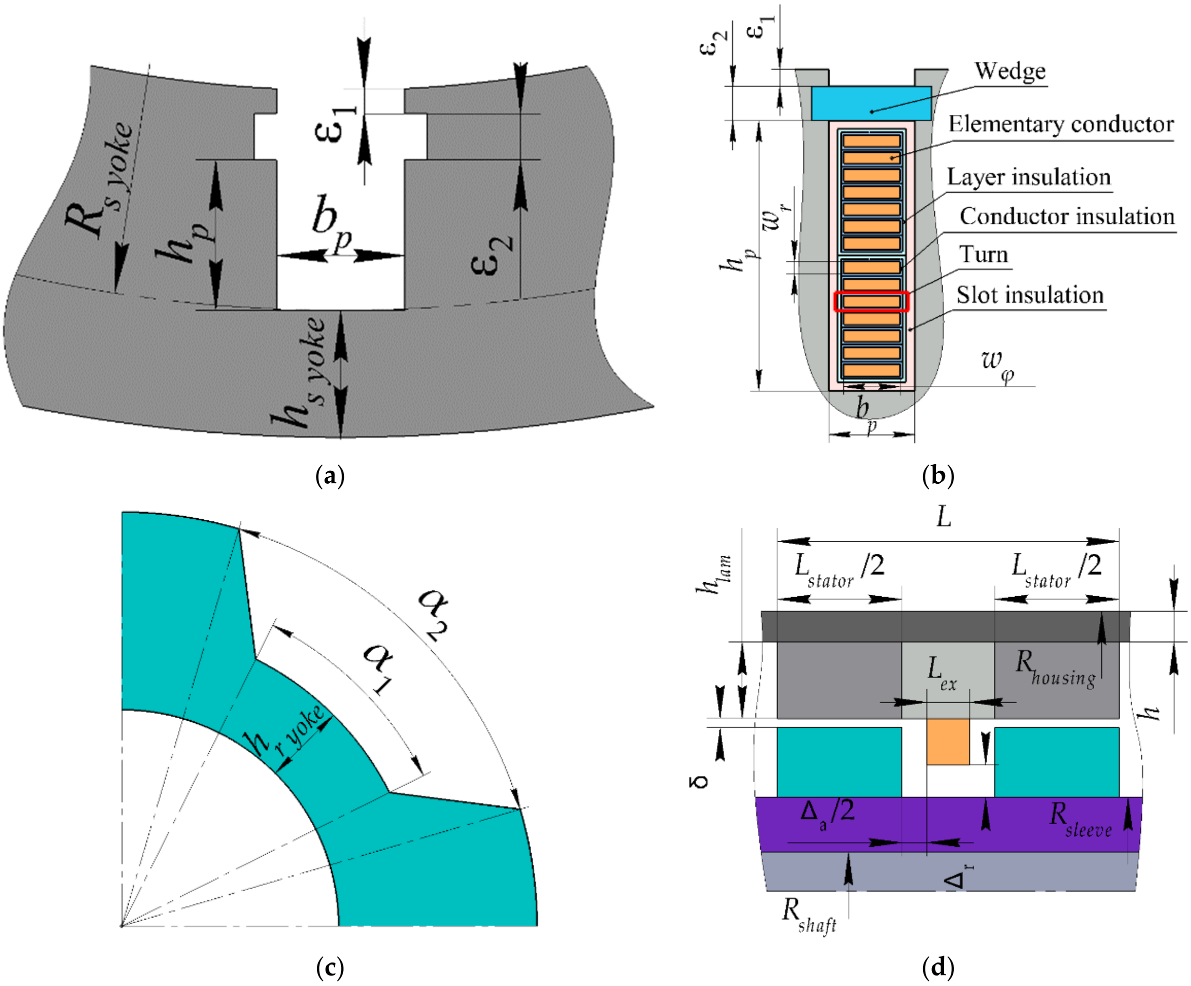

Figure 5. SHM geometric parameters. (**a**) Stator slot; (**b**) stator winding; (**c**) rotor core; (**d**) other dimensions.

Table 2. Some geometric parameters fixed during the optimization.

Parameter	Value
Machine length without end winding parts L, mm	302.5
Length of one stator stack	151.25
Stator housing radius, mm	267
Axial clearance between excitation winding and rotor, Δ_a, mm	29
Radial clearance between field winding and rotor Δ_r, mm	22
Shaft radius R_{shaft}, mm	40
Stator lamination yoke $h_{s\ yoke}$, mm	21
Rotor lamination yoke $h_{r\ yoke}$, mm	17
Stator wedge thickness, ε_2, mm	2
Stator unfilled area thickness, ε_1, mm	3

All of these determine other geometric parameters of the rotor and stator lamination including the inner rotor lamination radius that is the radius of the rotor sleeve. For example, the outer radius of stator lamination is determined by the outer housing radius and the housing thickness.

Table 3. Geometric parameters varied during the optimization.

Parameter	Initial Design	Optimized Design
Housing thickness h, mm	20	25.7
Total stator stacks length L_{stator}, mm	210	228
Stator slot depth, h_p, mm	36	30.6
Stator slot width, b_p, mm	7	7.5
Airgap width δ, mm	2	3.0
Rotor slot thickness, α_1, deg	36	36.7
Rotor slot thickness, α_2, deg	63	64.3
Angles of field weakening at operating points 1,2,3,4 electrical radians	0.5; 0.8; 0.4; 0.3	0.64; 0.91; 0.34; 0.17
Current ratio	5	5.95

The sizes of the armature wire w_x and w_y (see Figure 5b) necessary to compute the DC and eddy current loses in it [23] are determined according to Equation (10):

$$b_p = w_x + a_x;\, h_p = 2\cdot(w_y + \Delta w)\cdot N_{sec} + a_y, \tag{10}$$

where a_x = 1.51 mm, a_y = 1.8 mm, Δw = 0.31 mm are the constants taking into account the width of the slot insulation, layer insulation, impregnation, etc.

Only DC losses are assumed to be in the excitation winding. To calculate them, the copper filling factor 0.8 is adopted. Among parameters varied during the optimization, there are current angles measured from the middle of the rotor tooth in modes 1,2,3,4.

To reduce the number of the optimized parameters, the angle in operating point 5 is assumed to be the same as in operating point 4, the ratio of currents in in the excitation winding section, and the armature winding layer is assumed to be the same in all modes. Additionally, the ratio of the rotor slot widths α_2/α_1 (see Figure 5c) is assumed to be constant during the optimization. The mechanical losses are assumed to be mainly windage losses and proportional to the speed cubed. The mechanical losses at n_{max} are assumed to be 3.55 kW.

7. Optimization Results

Figure 6 shows the change of the electrical losses and current magnitude during optimization stage. Figure 7 depicts the simultaneous change of the symmetrized and non-symmetrized torque ripple. Figure 8 illustrates the change of the cost function value along the optimization.

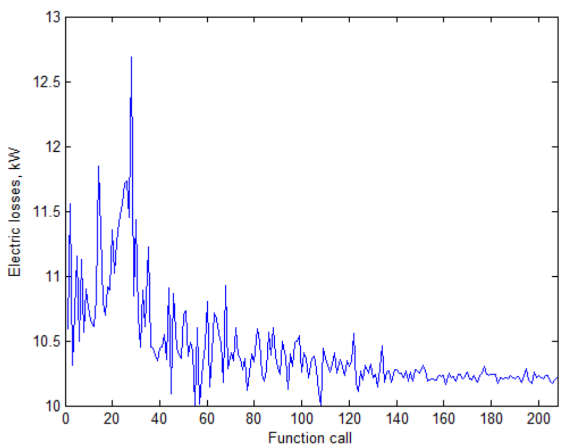

(**a**)

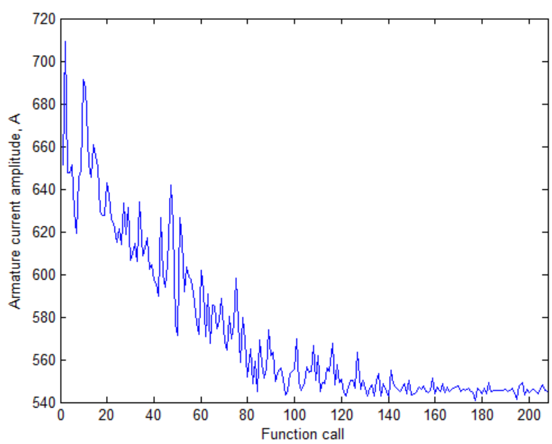

(**b**)

Figure 6. Change of the motor parameters during optimization. (**a**) Average losses; (**b**) maximum magnitude of the power winding current.

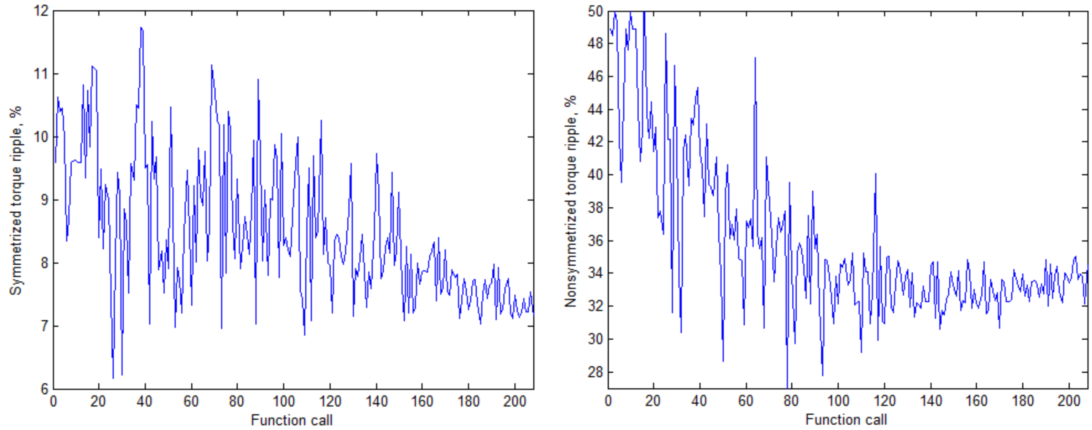

(**a**) (**b**)

Figure 7. Change of the motor parameters during optimization. (**a**) Symmetrized torque ripple; (**b**) nonsymmetrized torque ripple.

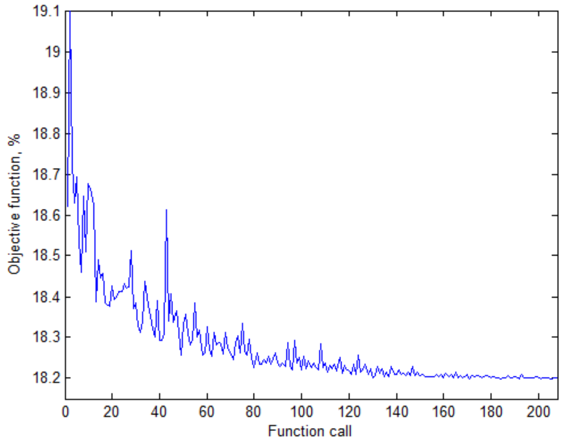

Figure 8. Variation of the cost function value according to (9) during optimization.

Figures 9 and 10 depict the geometry and induction value in the SHM before and after optimization. Table 4 shows the results of optimization.

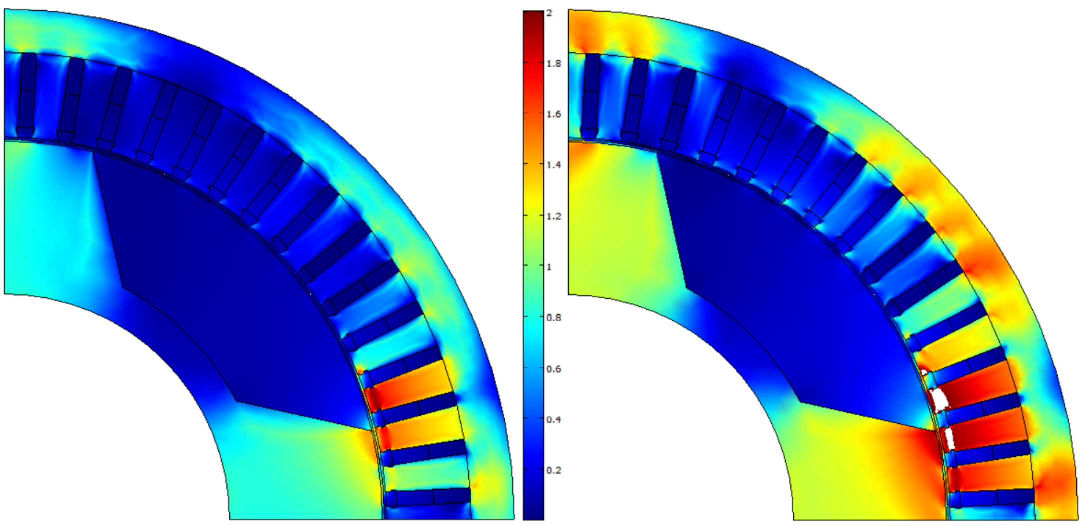

(**a**) (**b**)

Figure 9. The cross-section of the initial design of the synchronous homopolar motor and the magnitude plot of flux density (T); white areas mark the extreme saturation level (>2 T). (**a**) Operating point 1; (**b**) operating point 4.

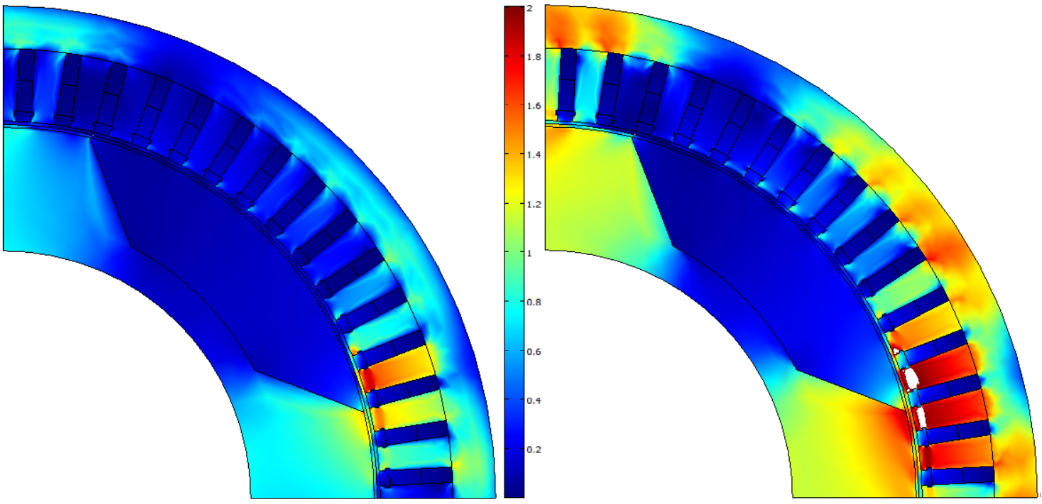

(**a**) (**b**)

Figure 10. The cross-section of the optimized design of the synchronous homopolar motor and the magnitude plot of flux density (T); white areas mark the extreme saturation level (>2 T). (**a**) Operating point 1; (**b**) operating point 4.

Table 4. Optimization results.

Parameter	Initial Design					Optimized Design				
Operating Point, *i*	**1**	**2**	**3**	**4**	**5**	**1**	**2**	**3**	**4**	**5**
Rotational speed n, rpm	4280	4280	2854	0	1427	4280	4280	2854	0	1427
Amplitude of the armature phase current I_{arm}, A	316	554	642	647	651	311	541	547	542	545
Efficiency, %	94.3	94.9	95.4	0.0	94.3	94.8	95.0	95.6	0.0	94.2
Output mechanical power P_{mech}, kW	185.3	−370.6	−370.6	0.0	185.3	185.3	−370.6	−370.6	0.0	185.3
Input electrical power, kW	196.6	−351.7	−353.7	8.3	196.4	195.4	−352.2	−354.4	8.9	196.8
Mechanical loss, kW	3.55	3.55	1.06	0.00	0.14	3.55	3.55	1.06	0.00	0.14
Armature DC copper loss, kW	1.79	5.51	7.39	7.50	7.60	2.48	7.53	7.67	7.55	7.62
Armature eddy-current copper loss, kW	1.15	3.96	3.25	0.00	0.83	0.59	2.25	2.16	0.00	0.60
Stator lamination loss, kW	4.14	4.63	3.99	0.00	1.68	2.87	3.39	3.64	0.00	1.65
Rotor lamination loss, kW	0.48	0.62	0.39	0.00	0.10	0.19	0.30	0.22	0.00	0.06
Excitation copper loss, kW	0.18	0.59	0.79	0.79	0.79	0.46	1.41	1.44	1.40	1.40
Total loss, kW	11.30	18.86	16.88	8.29	11.14	10.14	18.43	16.19	8.95	11.47
Average losses according to Formula (5)			12.43					12.02		
Number of turns in armature winding			5.93					6.68		
Power factor	0.986	−0.996	−0.924	1.000	0.920	0.994	−1.000	−0.927	1.000	0.905
Line-to-line voltage amplitude V_a, V.	728	749	699	14	383	718	755	825	16	468
Nonsymmetrized Torque ripple, %	48.9	33.7	23.4	23.4	23.4	33.9	25.9	18.8	19.0	19.0
Symmetrized torque ripple, %	9.59	7.40	4.90	5.04	5.03	7.21	5.47	3.77	3.91	3.91
Magnetic flux density in the housing and the sleeve, T	1.13	1.43	1.70	1.73	1.73	0.95	1.33	1.56	1.60	1.60

The following conclusions can be made by comparing motor parameters from Table 4 before and after optimization:

1. In the initial design, the magnetic flux density in the housing and the sleeve exceeds the chosen level of 1.6 T. After the optimization, the restriction of this value is fulfilled.
2. Average losses were reduced by (12.43 − 12.03)/12.43 = 3.2%;

3. The maximum current magnitude before optimization was 647 A at operation point 4, at zero speed and maximum torque. After optimization, the maximum current magnitude becomes at the operation point 3 at the speed n_g when transiting from the constant power to constant torque in generating mode. Thus, the maximum inverter current magnitude was reduced by $(647 - 547)/547$ = 15.5%.
4. Maximum symmetrized torque ripple (ripple at the shaft) occurs in the operation point 1 in the driving mode at maximum speed. After optimization its level was reduced by $(9.59 - 7.21)/7.21$ = 24.8%.

8. Conclusions

This article discusses the procedure and results of optimizing a 370 kW synchronous homopolar motor for driving subway train. The motor characteristics are optimized taking into account the subway train moving trajectory, namely acceleration and braking stages. A single-objective Nelder-Mead algorithm was used during our procedure. The number of motor operating points necessary to compute at one cost function call in the proposed approach is only five, which makes the computational efforts acceptable for the optimization.

The following optimization targets were selected: decreasing the average losses along the way from station to station, decreasing the installed power capacity of the traction inverter, and the reduction of the torque ripple. The optimization results show a significant improvement of the target parameters of the traction drive. Average motor losses were reduced by 3.2%. The required current of the solid-state inverter was reduced by 15.5%. The motor torque ripple was reduced by 24.8%.

Author Contributions: Conceptual approach, A.A., V.D. and V.P.; data curation, V.D. and V.K.; software, V.D. and V.P.; calculations and modeling, A.A., V.D., V.K. and V.P.; writing—original draft, A.A., V.D., V.K. and V.P.; visualization, V.D. and V.K.; review and editing, A.A., V.D., V.K. and V.P. All authors have read and agreed to the published version of the manuscript.

Funding: The research was performed with the support of the Russian Science Foundation grant (Project No 21-19-00696).

Institutional Review Board Statement: Not applicable.

Informed Consent Statement: Not applicable.

Data Availability Statement: Data are contained within the article.

Acknowledgments: The authors thank the editors and reviewers for careful reading and constructive comments.

Conflicts of Interest: The authors declare no conflict of interest.

References

1. Gundogdu, T.; Zhu, Z.-Q.; Chan, C.C. Comparative Study of Permanent Magnet, Conventional, and Advanced Induction Machines for Traction Applications. *World Electr. Veh. J.* **2022**, *13*, 137. [CrossRef]
2. Dianov, A. Highly Efficient Sensorless Multicontrol Mode Compressor IPMSM Drive with Seamless Transitions. *IEEE Trans. Power Electron.* **2022**, *37*, 9129–9137. [CrossRef]
3. Schulze, R. Reducing Environmental Impacts of the Global Rare Earth Production for Use in Nd-Fe-B Magnets, How Magnetic Technologies Much Can Recycling Contribute? Ph.D. Thesis, Technical University of Darmstadt, Darmstadt, Germany, December 2018. Available online: https://tuprints.ulb.tu-darmstadt.de/8301/7/Diss%20Rita%20Schulze%2015-12-2018.pdf (accessed on 4 November 2022).
4. Dong, S.; Li, W.; Chen, H.; Han, R. The status of Chinese permanent magnet industry and R&D activities. *AIP Adv.* **2017**, *7*, 1–17. [CrossRef]
5. Dmitrievskii, V.; Prakht, V.; Kazakbaev, V. Synchronous reluctance generator with ferrite magnets for wind turbine. *J. Phys. Conf. Ser.* **2018**, *1102*, 012041. [CrossRef]
6. De Lima, W.I.B. *Rare Earth Industry*; Elsevier: Amsterdam, The Netherlands, 2015.
7. Dmitrievskii, V.; Prakht, V.; Kazakbaev, V.; Anuchin, A. Comparison of Interior Permanent Magnet and Synchronous Homopolar Motors for a Mining Dump Truck Traction Drive Operated in Wide Constant Power Speed Range. *Mathematics* **2022**, *10*, 1581. [CrossRef]

8. Papini, F.; Osama, M. Electromagnetic Design of an Interior Permanent Magnet Motor for Vehicle Traction. In Proceedings of the 2018 XIII International Conference on Electrical Machines (ICEM), Alexandroupoli, Greece, 3–6 September 2018; pp. 205–211. [CrossRef]
9. Dianov, A. Optimized Field-Weakening Strategy for Control of PM Synchronous Motors. In Proceedings of the 2022 29th International Workshop on Electric Drives: Advances in Power Electronics for Electric Drives (IWED), Moscow, Russia, 26–29 January 2022; pp. 1–6. [CrossRef]
10. The First-Ever BMW iX3, PressClub Global, Article. Available online: https://www.press.bmwgroup.com/global/article/detail/T0310696EN/the-first-ever-bmw-ix3?language=enhttps://www.netcarshow.com/bmw/2021-ix3 (accessed on 4 November 2022).
11. Feustel, S.; Huebner, B.; Loos, D.; Merwerth, J.; Tremaudant, Y.; Vollmer, K. Rotor for Separately Excited Inner Rotor Synchronous Machine, Inner Rotor Synchronous Machine, Motor Vehicle and Method. U.S. Patent US20210006105A1, 7 January 2021. Available online: https://patents.google.com/patent/US20210006105A1 (accessed on 4 November 2022).
12. Raia, M.R.; Ruba, M.; Martis, C.; Husar, C.; Sirbu, G.M. Battery electric vehicle (BEV) powertrain modelling and testing for real-time control prototyping platform integration. In Proceedings of the 2021 23rd European Conference on Power Electronics and Applications (EPE'21 ECCE Europe), Ghent, Belgium, 6–10 September 2021; pp. 1–10. Available online: https://ieeexplore.ieee.org/document/9570616 (accessed on 4 November 2022).
13. Chu, W.Q.; Zhu, Z.Q.; Zhang, J.; Ge, X.; Liu, X.; Stone, D.; Foster, M. Comparison of electrically excited and interior permanent magnet machines for hybrid electric vehicle application. In Proceedings of the 2014 17th International Conference on Electrical Machines and Systems (ICEMS), Hangzhou, China, 22–25 October 2014; pp. 401–407. [CrossRef]
14. Illiano, E. Design of a Highly Efficient Brushless Current Excited Synchronous Motor for Automotive Purposes. Ph.D. Thesis, ETH-Zürich, Zürich, Switzerland, 2014. [CrossRef]
15. Orlova, S.; Pugachov, V.; Levin, N. Hybrid Excitation of the Axial Inductor Machine. *Latv. J. Phys. Tech. Sci.* **2012**, *49*, 35–41. [CrossRef]
16. Bindu, G.; Basheer, J.; Venugopal, A. Analysis and control of rotor eccentricity in a train-lighting alternator. In Proceedings of the 2017 IEEE International Conference on Power, Control, Signals and Instrumentation Engineering (ICPCSI), Chennai, India, 21–22 September 2017; pp. 2021–2025. [CrossRef]
17. Lorilla, L.; Keim, T.; Lang, J.; Perreault, D. Topologies for future automotive generators. Part I. Modeling and analytics. In Proceedings of 2005 IEEE Vehicle Power and Propulsion Conference, Chicago, IL, USA, 7 September 2005; pp. 74–85. [CrossRef]
18. Bianchini, C.; Immovilli, F.; Bellini, A.; Lorenzani, E.; Concari, C.; Scolari, M. Homopolar generators: An overview. In Proceedings of the 2011 IEEE Energy Conversion Congress and Exposition, Phoenix, AZ, USA, 17–22 September 2011; pp. 1523–1527. [CrossRef]
19. Dmitrievskii, V.; Prakht, V.; Anuchin, A.; Kazakbaev, V. Traction Synchronous Homopolar Motor: Simplified Computation Technique and Experimental Validation. *IEEE Access* **2020**, *8*, 185112–185120. [CrossRef]
20. Lashkevich, M.; Anuchin, A.; Aliamkin, D.; Briz, F. Control strategy for synchronous homopolar motor in traction applications. In Proceedings of the 43rd Annual Conference of the IEEE Industrial Electronics Society (IECON), Beijing, China, 29 October–1 November 2017; pp. 6607–6611. [CrossRef]
21. Dmitrievskii, V.; Prakht, V.; Anuchin, A.; Kazakbaev, V. Design Optimization of a Traction Synchronous Homopolar Motor. *Mathematics* **2021**, *9*, 1352. [CrossRef]
22. Prakht, V.; Dmitrievskii, V.; Anuchin, A.; Kazakbaev, V. Inverter Volt-Ampere Capacity Reduction by Optimization of the Traction Synchronous Homopolar Motor. *Mathematics* **2021**, *9*, 2859. [CrossRef]
23. Prakht, V.; Dmitrievskii, V.; Kazakbaev, V.; Anuchin, A. Comparative Study of Electrically Excited Conventional and Homopolar Synchronous Motors for the Traction Drive of a Mining Dump Truck Operating in a Wide Speed Range in Field-Weakening Region. *Mathematics* **2022**, *10*, 3364. [CrossRef]
24. Cupertino, F.; Pellegrino, G.; Gerada, C. Design of synchronous reluctance machines with multiobjective optimization algorithms. *IEEE Trans. Ind. Appl.* **2014**, *50*, 3617–3627. [CrossRef]
25. Krasopoulos, C.T.; Beniakar, M.E.; Kladas, A.G. Robust Optimization of High-Speed PM Motor Design. *IEEE Trans. Magn.* **2017**, *53*, 1–4. [CrossRef]
26. Fatemi, A.; Ionel, D.; Popescu, M.; Chong, Y.; Demerdash, N. Design Optimization of a High Torque Density Spoke-Type PM Motor for a Formula E Race Drive Cycle. *IEEE Trans. Ind. Appl.* **2018**, *54*, 4343–4354. [CrossRef]
27. Montonen, J.; Nerg, J.; Gulec, M.; Pyrhönen, J. A New Traction Motor System with Integrated-Gear: A Solution for Off-Road Machinery. *IEEE Access* **2019**, *7*, 113740–113750. [CrossRef]
28. Guo, S.; Zhao, H.; Wang, Y.; Yin, X.; Qi, H.; Li, P.; Lin, Z. A Design Technique of Traction Motor for Efficiency Improvement Based on Multiobjective Optimization. *World Electr. Veh. J.* **2021**, *12*, 260. [CrossRef]
29. Lin, F.; Li, X.; Zhao, Y.; Yang, Z. Control Strategies with Dynamic Threshold Adjustment for Supercapacitor Energy Storage System Considering the Train and Substation Characteristics in Urban Rail Transit. *Energies* **2016**, *9*, 257. [CrossRef]
30. Nelder, J.; Mead, R. A Simplex Method for Function Minimization. *Comput. J.* **1965**, *7*, 308–313. [CrossRef]
31. IEC. *Specifications for Particular Types of Winding Wires—Part 0-2: General Requirements—Enamelled Rectangular Copper Wire*; IEC 60317-0-2:2020; IEC: Geneva, Switzerland, 2020. Available online: https://webstore.iec.ch/publication/63495 (accessed on 1 November 2022).